Effect of non-ideally manufactured riblets on airfoil and wind turbine performance

Tiainen Jonna, Grönman Aki, Jaatinen-Värri Ahti, Pyy Lauri

DOI: 10.1016/j.renene.2020.03.102

Effect of non-ideally manufactured riblets on airfoil and wind turbine performance

Jonna Tiainen[a,*], Aki Grönman[a], Ahti Jaatinen-Värri[a], Lauri Pyy[a]

[a] *LUT University, P.O. Box 20, FI-53851 Lappeenranta, Finland*

Abstract

Riblets are a passive flow control method, which can be used for drag reduction, especially with small wind turbines that have a low Reynolds number. Riblet manufacturing, however, is a challenging task and the required production quality can cause extra barriers in terms of time and costs. If a relatively low-quality riblet structure could be successfully utilized in airfoils, it could enable wider adaptation of this particular flow control method. Public literature lacks studies that examine the applicability of non-ideally manufactured riblets on the ribleted airfoil. Therefore, in this study, Constant Temperature Anemometer and Particle Image Velocimetry are used to reveal the effect of non-ideal riblets on their performance and the flow field downstream of the airfoil. The measurements with a varying Reynolds number and incidence angle are conducted in the wind tunnel. The results indicate that, in the optimum conditions for the riblet design, the riblets reduce drag, thicken the boundary layer, reduce turbulence intensity, and weaken the mixing process. It is further demonstrated, that low-quality riblets have the potential to improve the performance of wind turbines, even when the riblet quality is lower than typically used.

Keywords: Boundary layer, Drag reduction, Flow control, Wake, Wind turbine

*Corresponding author
Email address: jonna.tiainen@lut.fi (Jonna Tiainen)

1. Introduction

Global wind energy installations have increased dramatically in the early 21st century and their capacity is expected to continue its growth well into the future [1]. The small-scale wind turbine market is also growing, although not as much as that of large turbines [2]. One drawback of smaller turbines is the decreased performance due to the low Reynolds numbers, which are caused by low wind speeds and the small physical size of the turbine.

One solution that can help to meet low Reynolds number challenges are riblets, which are small streamwise aligned grooves that shift turbulent vortices farther away from the surface [3]. The riblets reduce drag when their tip is as sharp as possible [4], and their spacing is small enough (dimensionless riblet spacing $s^+ = (su_\tau)/\nu < 30$) or otherwise one streamwise vortex would fit into the groove between the riblets resulting in increased drag [5]. The optimal ratio between the riblet height and spacing is 0.5 as the breakdown of riblet performance is associated with spanwise quasi-two-dimensional vortices below $y^+ \approx 30$ [6]. Riblets have shown their potential in drag reduction in adverse pressure gradient flows [7] and low-Reynolds-number flows [8]. The experimental results of Choi [9] indicated that an increase in viscous sublayer thickness due to riblets shifted the entire velocity profile from the viscous sublayer to the outer layer upwards. The increase in viscous sublayer thickness resulted in reduced turbulence energy production, reduced turbulence intensity, and reduced turbulent drag in the near-wall region [9].

A limited number of studies are available on ribleted airfoils, either with symmetric [10, 11, 12] or non-symmetric airfoils [13, 14]. Approximately 16% drag reduction was reported for symmetric airfoils by Sundaram et al. [11] and the maximum measured drag reduction was 4-6% with non-symmetric airfoils. It was further observed that a non-optimal riblet design can lead to increased drag of up to 10-12%. A similar finding was also made by Han et al. [12] with 4.3% maximum drag decrease and 15.8% maximum drag increase. The measurements of Lietmeyer et al. [15] with ground and laser-structured riblets

indicated that wall shear stress additionally decreased by 1% when the riblet tips were sharper, the geometry was more trapezoidal, and the riblet height-to-spacing ratio was increased towards the optimum value of 0.50 from 0.25 to 0.49. However, the manufacturing of ideal riblets can be time-consuming, challenging and expensive, which can cause additional barriers to their use. One solution that is fast and economically affordable is nanosecond laser ablation [16]. However, the quality of riblets cannot match its close competitors and, as discussed above, the quality can have a marked influence on the effectiveness of the riblets.

Besides the quality of the riblets, their performance depends on the Reynolds number. Spalart and McLean [17] discussed that riblet effectiveness is lower at higher Reynolds numbers in full-scale applications than at lower Reynolds numbers in small-scale experiments. In the study of Han et al. [12], drag reduction occurred at a lower Reynolds number, whilst drag increase occurred at a higher Reynolds number. Riblet effectiveness was also studied by Gatti and Quadrio [8], who concluded in their DNS (Direct Numerical Simulation) study that the performance of riblets improves with decreasing Reynolds numbers. Before the study of Gatti and Quadrio [8] was published, it was assumed that drag-reduction performance decreases with increasing Reynolds numbers as a function of a power law. Gatti and Quadrio [8] argued that the power law assumption had no physical background, and they proposed a dimensionless relation between the Reynolds number and drag-reduction rate, which included the term 'vertical shift of the logarithmic region' in the velocity profile.

In addition to the Reynolds number, the incidence angle of the airfoil affects riblet performance. The results of Viswanath [18] and Sundaram et al. [11] showed improved drag reduction with increased incidence. The findings of Nieuwstadt et al. [19] suggested that the riblets perform better at adverse pressure gradients, i.e. at higher incidence angles.

In the case of wind turbines, ice, fouling and wearing may affect riblet effectiveness in real life conditions. Lietmeyer et al. [20] examined the deposition of dust particles on ribleted NACA 6510 compressor blades. The results of Li-

etmeyer et al. indicated that the contamination behavior was similar between the laser-structured riblet surface and the smooth airfoil surface. However, on the riblet surface where the ideal riblets were produced on a foil, the particles were deposited more on the sharp riblet tips than in the grooves. Lietmeyer et al. expected that the contamination would not strongly affect riblet effectiveness, as the tips are more contaminated than the grooves in the case of ideal riblets. Based on the findings of Lietmeyer et al., it seems that the tips with ideal sharpness might be more prone to fouling than the less sharp tips.

In addition to the drag reduction performance, the flow phenomenon downstream of the riblets is important, especially in the case of wind farms where the downstream turbines are affected by the upstream flow field. However, there is a lack of studies regarding the detailed effect of riblets on the flow field downstream of their location. To the authors' knowledge, the works of Caram and Ahmed [10] (chord Reynolds number of 250,000) and Han et al. [12] (chord Reynolds number of 17,000 and 36,000) are the only ones that provide an evaluation of flow phenomena downstream from the ribleted airfoil at different locations, both with zero incidence. Caram and Ahmed [10] found that the growth of the wake was similar with both ribleted and smooth airfoils, although the wake shear stress and turbulence intensity varied from each other. Han et al. [12] noticed that the velocities behind the ribleted airfoil were faster in some areas than with the smooth airfoil when the riblets reduced drag, while an opposite observation was made when the riblets increased drag.

From the background presented, it can be observed that there are currently no studies, which cover the performance of non-ideal riblets at different Reynolds numbers and incidence angles and examine their effects on downstream flow field and turbine performance. The novelties of this study are: (1) a detailed performance and fluid dynamic analysis of non-ideal riblets, (2) combined examination of the effects of Reynolds number and incidence on the flow field downstream from the ribleted airfoil, and (3) estimation of the non-ideal riblet's effect on wind turbine performance. The hypothesis is that the riblets, manufactured economically and quickly using a nanosecond pulse laser, can reduce drag and

turbulence intensity despite their non-ideal quality, so they could be an economically feasible and potential flow control method to improve wind turbine performance. It is also expected that the thickened boundary layer due to the riblets increases the width of the wake, resulting in a stronger and wider wake behind the airfoil.

In this study, three incidence angles and two Reynolds numbers are tested both with a smooth and ribleted airfoil in a wind tunnel with Constant Temperature Anemometer (CTA) traverses and Particle Image Velocimetry (PIV). The riblets are manufactured using nanosecond laser ablation on one side of the symmetric NACA 0024 profile. Although, symmetric NACA airfoils are not used in modern Horizontal Axis Wind Turbines (HAWTs) they provide a good case for research, as was discussed by Chamorro et al. [14]. They are also the most used airfoil profiles in vertical axis wind turbines (VAWTs) [21], and recently NACA 0024 profile has also been used as a floating deflector in a tidal kinetic turbine [22].

The article is constructed so that first the design of riblets and the experimental setup are presented, then the effect of riblets is compared with a smooth airfoil in the results section including analyses of boundary layer and downstream flow field behaviors. At the end of the results section, the performance change of a HAWT is modelled with non-ideal riblets over several tip speed ratios. Finally, conclusions are drawn in the last section.

2. Experimental Setup

The studied airfoil is a symmetric NACA 0024 profile with a chord length of 125 mm. The experiments were conducted in the wind tunnel of the Laboratory of Fluid Dynamics at LUT University, Finland. Flow velocity can be varied between 10 and 30 m/s, resulting in the values of the chord Reynolds number ranging from 83,000 to 248,000. The blockage ratio (the ratio between the projected area of the airfoil and the cross-sectional area of the wind tunnel test section) is 7%. The value is within the range 1-10% recommended by Barlow

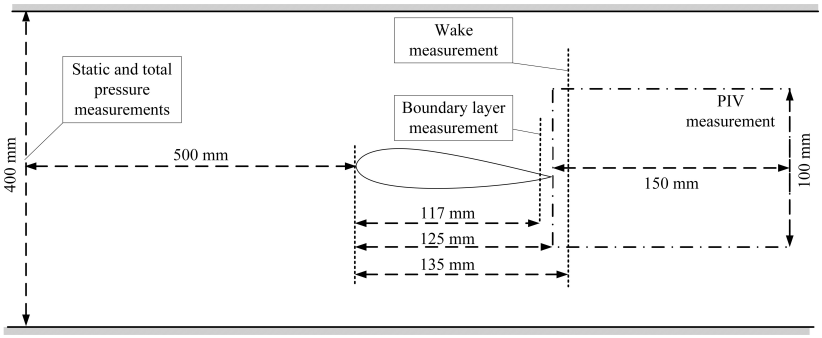

Figure 1: Schematic view of the test section with the NACA 0024 profile.

et al. [23], and therefore, no blockage correction is applied in this study as it would be negligible.

The following experiments were performed: the measurement of turbulence intensity, flow field measurements with CTA at the locations of 117 mm (0.94c) and 135 mm (1.1c) from the airfoil leading edge, and flow field measurement with PIV downstream of the airfoil trailing edge. The locations of the flow field measurements are shown in Fig. 1. Additionally, static and total pressures at the inlet of the test section (500 mm from the airfoil leading edge) were measured using static pressure measurement taps and Pitot-tubes.

The measurements were performed at the Reynolds numbers of 174,000 (low) and 220,000 (high), and at incidences in the range of $-5 \ldots +5°$. The definition of incidence is sketched in Fig. 2. The selected Reynolds numbers are below and above the flat plate's critical Reynolds number of 200,000, below which greater friction losses should occur [24]. The riblets are known to perform better on the airfoil suction side [20], but the selection of the incidence range was based on the aim of distinguishing the performance of the riblets at both positive and negative incidences without severe flow separation.

2.1. Riblets

The riblets were designed at Leibniz University Hannover, Germany. The design parameters and their definitions are shown in Table 1, which also shows

Table 1: Design parameters of riblets and an example of the manufactured riblets.

Angle	30°
Height	0.149 mm
Location	$65 - 90\%c$
Shape	Trapezoidal
Spacing	0.298 mm

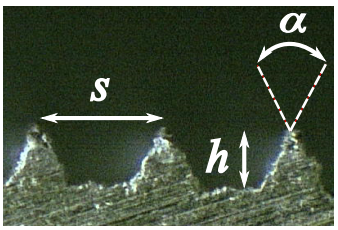

the configuration of the riblet surface. The design is based on the knowledge of wall shear stress distribution along the airfoil surface, which was gained from CFD (Computational Fluid Dynamics) simulations. The numerical results were validated quantitatively against the measured static pressure distribution along the airfoil surface and qualitatively against the results of oil film visualization. The aim of the design was to locate the riblets with the optimum height-to-spacing ratio of 0.5 in the turbulent flow region.

The riblets were manufactured on one side of the symmetric airfoil using nanosecond laser ablation in the Laboratory of Laser Processing at LUT University. The applicability of the nanosecond laser ablation in the manufacture of riblets and the quality of the manufactured riblets were studied by Kaakkunen et al. [16, 25]. The results of Kaakkunen et al. [16] indicated that nanosecond laser ablation is a faster and more economical manufacturing method than grinding or ultra-short pulse lasers, but the quality is lower.

The angle of riblets (α) varied in the range of $50 - 65°$ [16], and on average the angle was 93% greater than the designed one. The height of riblets varied in the range of $0.106 - 0.191$ mm [16], on average the height was equal to the designed one, and the height-to-spacing ratio varied in the range of $0.36 - 0.64$ equaling the optimum of 0.5 on average. The designed location for the riblet surface on the airfoil was the turbulent region $65 - 90\%$ of the chord length and the actual location after manufacturing was $62 - 86\%$ of the chord length. As the contamination of the riblets starts from the riblet tips [20], the larger riblet angles also demonstrate riblet performance after contamination and erosion.

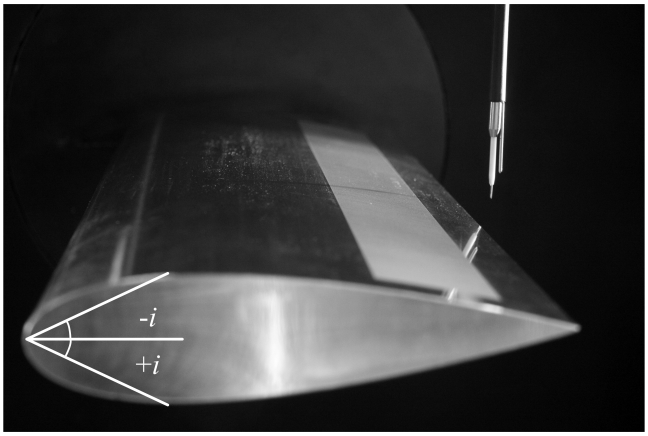

Figure 2: CTA probe used for flow field measurements and the definition of incidence.

2.2. Constant Temperature Anemometer

A Constant Temperature Anemometer was used to measure flow fields in the boundary layer and wake. The measurement setup consisted of a miniature wire probe (type 55P11 from Dantec, shown in Fig. 2), a CTA module (56C01 from Dantec) and a data acquisition system (NI cDAQ-9178 from National Instruments). LabVIEW (National Instruments) was used for data acquisition. The effect of the wind tunnel walls was eliminated by measuring in the middle of the tunnel. The spanwise length of the airfoil profile (and the wind tunnel width) was 250 mm and, based on oil film visualization, the flow field in the middle of the tunnel was 2-dimensional.

CTA was calibrated over the velocity range from 7 to 30 m/s. The number of samples was 1,000 and sampling rate 10 kHz. Turbulence intensity was calculated as a ratio of velocity fluctuation component (standard deviation) u_{rms} and mean velocity component U_{mean}:

$$Tu = \frac{u_{\mathrm{rms}}}{U_{\mathrm{mean}}} \cdot 100\%. \tag{1}$$

The value of turbulence intensity in the wind tunnel was 2.2%, which is between the onshore [26] and offshore [27] turbulence intensities. The maximum relative uncertainties of turbulence intensity and other variables with a 95% confidence

Table 2: Maximum relative measurement uncertainty with a 95% confidence interval.

Turbulence intensity	0.2%
Velocity	0.8%
Friction velocity	3.3%
Wall shear stress	4.7%
Local friction coefficient	6.8%

interval are shown in Table 2. The uniformity of the flow field was verified by traversing the CTA probe in the middle of the test section in a vertical direction.

2.3. Particle Image Velocimetry

Particle Image Velocimetry was utilized to capture the velocity field after the trailing edge of the airfoil. The PIV system was set up in a planar way using one camera, as the z velocity component towards the camera was considered to be almost non-existent.

The PIV system (shown in Fig. 3) was made by LaVision. The system utilized the sCMOS camera with a 50 Hz frame rate. The size of the CMOS chip was 2,560 x 2,160 pixels with a pixel size of 6.5 x 6.5 μm^2. The digital output was 16 bits. The inter-framing time between two images was 120 ns. The lens used in the measurement was a Canon EF 50 mm with f/1.4 aperture.

The laser unit was Litron's Nano T-180 Nd:YAG double cavity laser. The maximum pulse energy was 180 mJ and the maximum frequency was 15 Hz, which was also the limiting factor for measuring frequency. The laser unit was attached to the laser guiding arm with laser sheet optics. The laser sheet optics consisted of two spherical lenses and a divergence lens of $f = -10$ mm.

The laser unit and camera were triggered by a PTU X programmable timing unit. For seeding Di-Ethyl-Hexyl-Sebacate, DEHS was used with an aerosol generator. DEHS particles had a mean size of roughly 1 mm and below. Particle images were recorded and analyzed with DaVis 10.0.3 software.

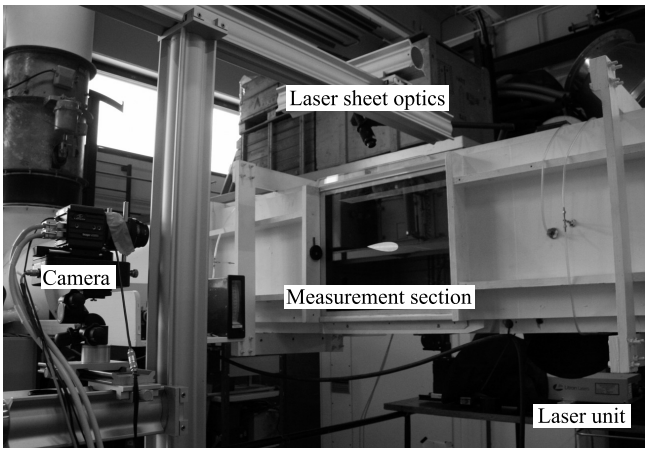

Figure 3: PIV measurement setup.

The sample size of 500 image pairs was optimized to fulfill the requirements of converged results and minimum computational time. The time delay, dt, between particle images was 43 and 55 μs for the investigated Reynolds numbers of 174,000 and 220,000, respectively.

For post-processing the particle images, 32 x 32 pixel interrogation window size was chosen with 25% overlap thus making the effective size of the interrogation windows 24 x 24 pixel. The measurement area was originally 300 mm x 250 mm but it was cropped due to the constraints in the optical access to the wind tunnel. Laser sheet shot from the ceiling of the wind tunnel created high reflection on the top of and shadow underneath the airfoil. Thus, it was decided to use the area presented in Fig. 1 as the (effective) measurement area. The scale factor after calibration was 8.6 pixels/mm which leaves 54 x 36 interrogation windows to the measurement area and is the (effective) resolution of the PIV measurement.

3. Results and Discussion

3.1. Boundary layer

The velocity profiles measured using the CTA are presented for low and high Reynolds numbers in Figs. 4 and 5. As the riblet height is of the order of the

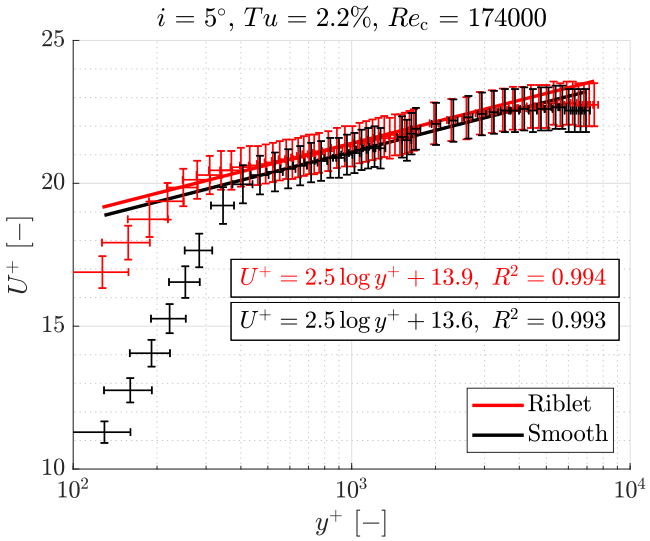

Figure 4: Dimensionless boundary layer profile at the low Reynolds number of 174,000 and an incidence of 5° for riblet (red) and smooth (black) surfaces. The law of the wall and R-squared values are shown for both surfaces.

viscous sublayer thickness, the measurements reach the buffer layer. The results in Figs. 4 and 5 indicate that the riblets shift the velocity profile upwards as also found by Choi [9]. Higher velocities and the thickening of the sublayer due to the riblets were also observed by Sundaram et al. [11].

The upward shift is a result of the increased viscous sublayer thickness due to riblets, which corresponds to drag reduction [5]. The effect of riblets is stronger at lower Reynolds numbers. The finding of the stronger influence of riblets at lower Reynolds numbers agrees with the findings published by Gatti and Quadrio [8], and Spalart and McLean [17], who stated that the riblets decrease drag more at low Reynolds numbers than at high ones. The increased thickness of the viscous sublayer shifts the logarithmic region upwards, resulting in the increased value of constant B in the law of the wall [5].

In the present study, the riblets reduce turbulence intensity near the surface (Fig. 6), as in the studies published by Choi [9] and Lee and Choi [28]. The reduction is especially evident at the lower Reynolds number, as expected. As

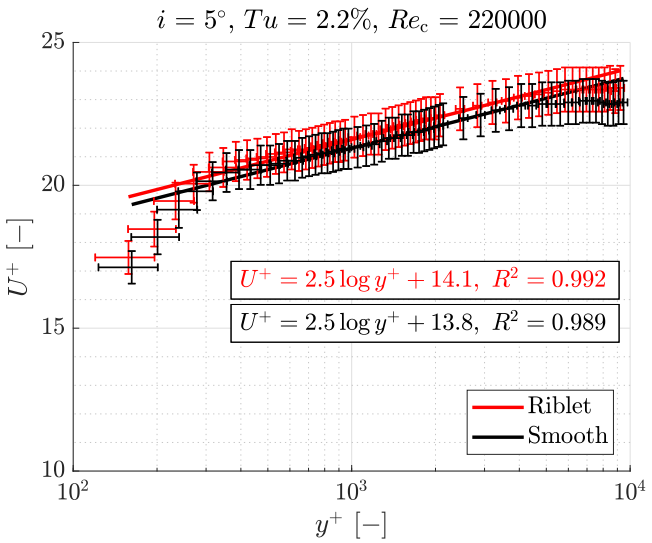

Figure 5: Dimensionless boundary layer profile at the high Reynolds number of 220,000 and an incidence of 5° for riblet (red) and smooth (black) surfaces. The law of the wall and R-squared values are shown for both surfaces.

in the review of Viswanath [18], the reduction of turbulent kinetic energy can be observed in the spectral distribution of energy from the CTA measurement at the location of 117 mm from the airfoil leading edge (Fig. 7). In the inertial subrange, the energy spectral density distribution follows the Kolmogorov -5/3 law. Because the measurements do not reach the viscous sublayer, the sudden drop describing the viscous sublayer is not visible in the distribution at high wavenumbers. It is also known that reduced turbulence intensity weakens the mixing out of the wake [29].

Table 3 shows the friction velocity u_τ, wall shear stress $\tau_w = \rho u_\tau^2$, and local friction coefficient $c_f = (2u_\tau^2)/U_\infty^2$ values. In this study, the friction velocity is estimated based on the measured data in the logarithmic region, and this information is used to estimate the wall shear stress and local friction coefficient. In the calculation of friction velocity, it is assumed that the tenth measurement point from the surface lies in the logarithmic region (this can be seen in Figs. 4

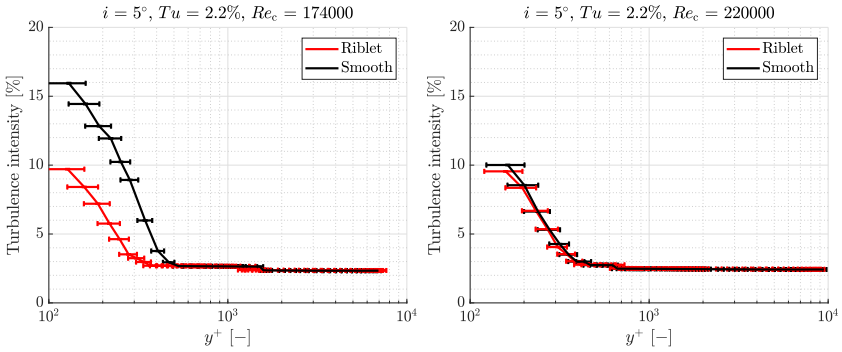

Figure 6: Turbulence intensity profiles at the Reynolds numbers of 174,000 (left) and 220,000 (right), and an incidence of 5° at 117 mm from the airfoil leading edge for riblet (red) and smooth (black) surfaces.

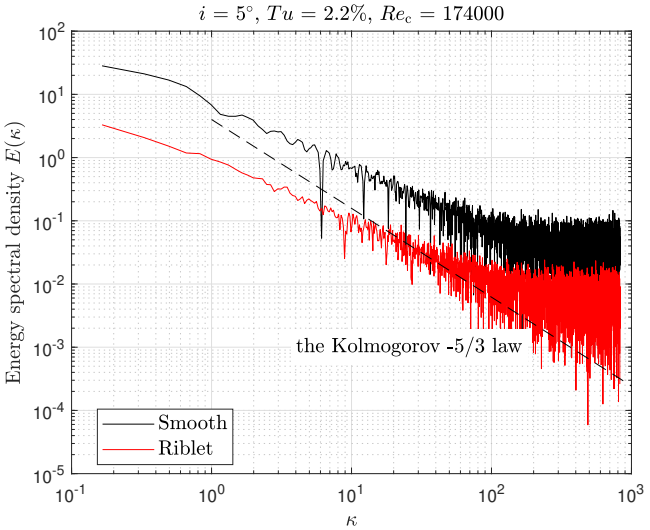

Figure 7: Energy spectrum at the Reynolds number of 174,000 and an incidence of 5° at 117 mm from the airfoil leading edge for riblet (red) and smooth (black) surfaces.

Table 3: Experimental results of friction velocity, wall shear stress, and friction coefficient on smooth and riblet surfaces, 117 mm from the airfoil leading edge.

i		$+5°$	$+5°$	$0°$	$0°$	$-5°$	$-5°$
Tu		2.2%	2.2%	2.2%	2.2%	2.2%	2.2%
Re_c		174,000	220,000	174,000	220,000	174,000	220,000
u_τ	smooth	0.931	1.167	0.962	1.169	0.987	1.211
u_τ	riblet	0.915	1.136	0.965	1.180	0.987	1.227
u_τ	riblet vs. smooth	−1.7%	−2.6%	+0.2%	+0.9%	±0%	+1.3%
τ_w	smooth	1.019	1.618	1.102	1.617	1.148	1.734
τ_w	riblet	0.994	1.509	1.085	1.640	1.133	1.769
τ_w	riblet vs. smooth	−2.4%	−6.8%	−1.5%	+1.4%	−1.3%	+2.0%
c_f	smooth	0.00398	0.00385	0.00415	0.00403	0.00434	0.00411
c_f	riblet	0.00385	0.00365	0.00417	0.00410	0.00434	0.00422
c_f	riblet vs. smooth	−3.3%	−5.2%	+0.5%	+1.8%	±0%	+2.7%

and 5) and friction velocity is calculated with the iterative method as follows

$$\frac{u}{u_\tau} = \frac{1}{\kappa} \log\left(\frac{u_\tau y}{\nu}\right) + B, \tag{2}$$

where κ is 0.4, B is 5.1, and u and y are velocity and distance from the surface in the tenth measurement point.

The riblets have been designed for an incidence of $+4°$, so they perform best at a positive incidence ($+5°$) as shown in Table 3. There is no observable difference in the wake between the incidences of $+4°$ and $+5°$. At the incidence angle of $+5°$, riblets reduce wall shear stress by 2.4% at the Reynolds number of 174,000 and by 6.8% at the Reynolds number of 220,000. The corresponding changes in the friction coefficient are -3.3% and -5.2%, respectively. The riblets seem to perform slightly better at a higher Reynolds number, but the measurement uncertainties of friction velocity, wall shear stress and local friction coefficient are higher than that of turbulence intensity. At the incidence of $+5°$, friction velocity decreases by $1.7 - 2.6\%$ depending on the Reynolds number. The reductions in friction velocity and wall shear stress in the present study

are of the same order of magnitude as in the study published by Choi [9]. The results further indicate that the riblet effectiveness is not as sensitive on the tip angle as on the height-to-spacing ratio or trapezoidal shape, as the height-to-spacing ratio and trapezoidal shape were close to the design, but the tip angle was 93% greater than the designed one.

3.2. Boundary layer and wake near the airfoil trailing edge

As shown above, the riblets perform best at the positive incidences ($+4 \ldots +5^\circ$), which is also evident in Figs. 8, 9, and 10, where the Reynolds stress, $u'u'$ is shown at the incidences of $+5^\circ$, 0°, and -5°, respectively. On the left of Figs. 8, 9, and 10, the Reynolds stress is shown in the airfoil boundary layer at the location of 94% of the chord length (117 mm from the airfoil leading edge). On the right of Figs. 8, 9, and 10, the Reynolds stress is shown in the wake at the location of 108% of the chord length (10 mm behind the airfoil trailing edge). On the right of Figs. 8, 9, and 10, the airfoil trailing edge is located 10 mm upstream at the vertical location of 0 mm.

The Reynolds stress distribution in the boundary layer in Fig. 8 indicates that the riblets reduce Reynolds stress and turbulence intensity. On the right of Fig. 8, the reduction in Reynolds stress is visible on the airfoil suction side (upper surface, vertical location > 0 mm), but not as strongly as in the boundary layer (on the left of Fig. 8) due to mixing. The maximum reduction in Reynolds stress is about 80% in the boundary layer, and about 30% in the wake. It is also worth noting that the wake asymmetry is slightly increased due to riblets.

As the riblets perform better on the airfoil suction side, they have a minor effect on the flow field in the boundary layer of the symmetric airfoil at an incidence of 0° on the left of Fig. 9, where the riblets seem to reduce the Reynolds stress slightly (by up to 30%). However, according to Table 3, the wall shear stress decreased by 1.5% and the friction coefficient increased by 0.5% at the lower Reynolds number and the incidence of 0°, whereas the wall shear stress increased by 1.4% and the friction coefficient increased by 1.8% at the higher Reynolds number and the incidence of 0°. In the wake (on the right

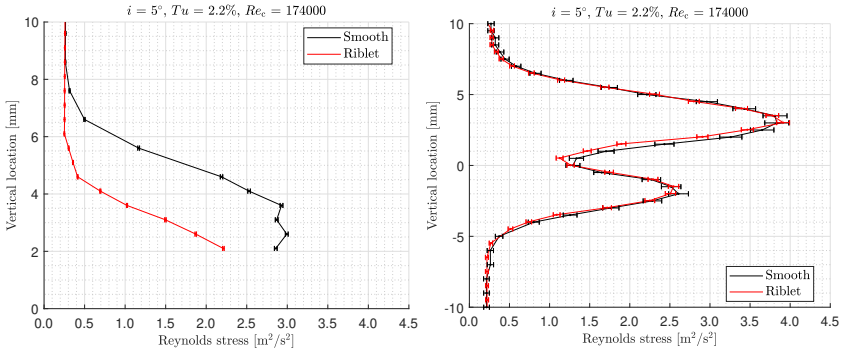

Figure 8: Reynolds stress at 94% (left) and 108% (right) of the chord length. Riblets work as designed at $i = +5°$, and reduce Reynolds stress. The reduction in Reynolds stress is still visible at 10 mm behind the airfoil trailing edge on the suction side (vertical location > 0 mm).

of Fig. 9), a noticeable increase (the maximum increase is around 15%) in the peak Reynolds stresses can be detected. This increase can be explained by the increased drag, resulting from the earlier transition from laminar to turbulent flow when the incidence is reduced. The riblets are not able to cancel out this drag increase. The role of the riblets in wake asymmetry is also negligibly small at an incidence of 0°, which can be explained by the reduced riblet performance under these conditions.

On the airfoil pressure side, the riblets do not affect the flow field in the upper boundary layer (left of Fig. 10). Interestingly, the Reynolds stresses experience an increase in the wake below the mean-line (vertical location < 0 mm, right of Fig. 10) when the riblets are located at the pressure surface. This behavior is not visible in Fig. 8 and must therefore be related to the riblet positioning. One explanation for the noticed phenomenon could be that the riblets are acting as roughness elements on the pressure side, which then cause the suction side flow to become more asymmetric.

3.3. Wake development

This section describes the development of the wake downstream of the airfoil trailing edge. The wake development can be illustrated with the Reynolds stress

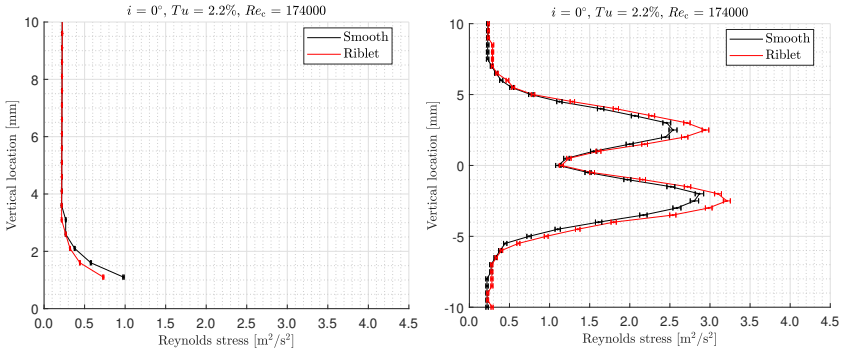

Figure 9: Reynolds stress at 94% (left) and 108% (right) of the chord length. Riblets work only a little at $i = 0°$, and reduce Reynolds stress slightly in the boundary layer, but they cannot cancel out the drag increase resulting from the earlier transition.

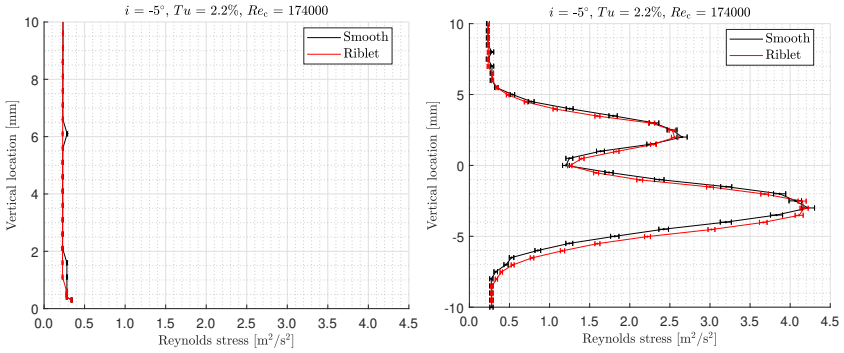

Figure 10: Reynolds stress at 94% (left) and 108% (right) of the chord length. Riblets do not work at $i = -5°$, and do not change Reynolds stress.

contours from the PIV measurements. Based on the data in Table 3, two cases with high wall shear stress reduction and high wall shear stress increase are chosen for demonstration. Figure 11 shows the Reynolds stress contours in the wake of the smooth airfoil (top left), in the wake of the riblet airfoil (top right), and the relative difference between the riblet and smooth airfoils (bottom) in the case of the high wall shear stress reduction. The airfoil trailing edge is located at the vertical location of 0 mm. The negative values of the difference in Reynolds stress indicate that the riblets reduce turbulence on the airfoil suction side (upper surface, vertical location between 0 and 5 mm). As the turbulence vortices are shifted by the riblets away from the surface, the increase

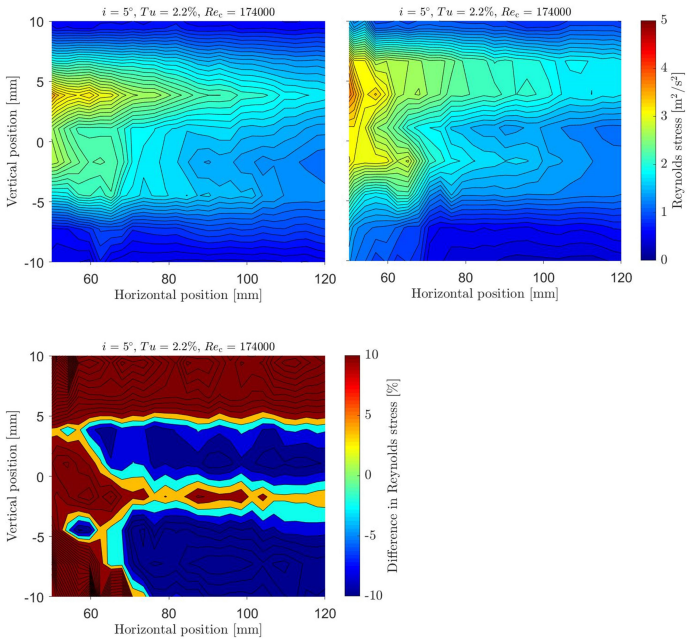

Figure 11: The contours of Reynolds stress in the wake of the smooth airfoil (top left), in the wake of the riblet airfoil (top right), and the relative difference between the riblet and smooth airfoils (bottom) at the Reynolds number of 174,000 and an incidence of 5°.

in Reynolds stress is observable above the vertical location of 5 mm. The data between the airfoil trailing edge and the location of 50 mm downstream were not captured with the PIV due to the reflection from the airfoil surface.

Figure 12 shows the Reynolds stress contours in the wake of the smooth airfoil (top left), in the wake of the riblet airfoil (top right), and the relative difference between the riblet and smooth airfoils (bottom) in the case of the high wall shear stress increase. As in Fig. 11, the airfoil trailing edge is located at the vertical location of 0 mm. The positive values of the difference in Reynolds stress indicate that the riblets increase turbulence on the airfoil pressure side (upper surface, vertical location > 0 mm), as the riblets act as roughness elements. Below the vertical location of 0 mm, the Reynolds stress is reduced. As the riblets are located on the airfoil pressure side, it seems that the reduced Reynolds stress is a result either of postponed transition from laminar to turbulent on the

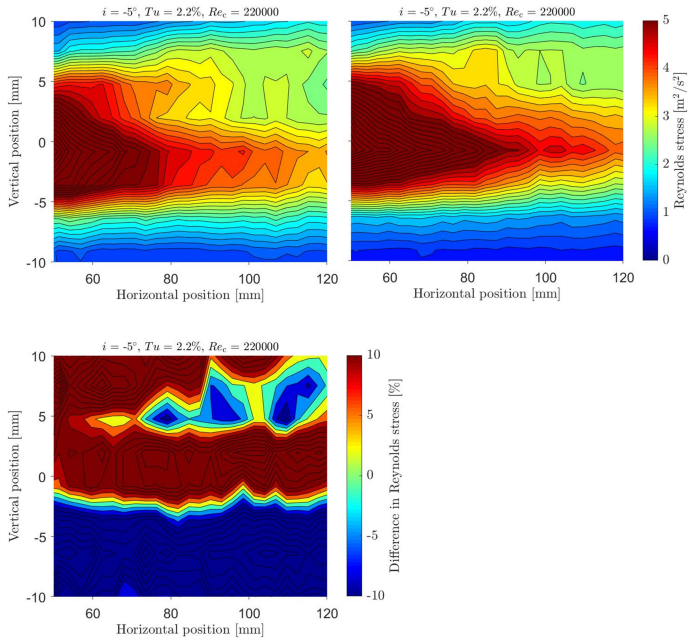

Figure 12: The contours of Reynolds stress in the wake of the smooth airfoil (top left), in the wake of the riblet airfoil (top right), and the relative difference between the riblet and smooth airfoils (bottom) at the Reynolds number of 220,000 and an incidence of $-5°$.

airfoil suction side or of a more asymmetric flow field.

In addition to the Reynolds stress contours, the wake development can be illustrated by wake thickness distribution. The data presented is taken from the CTA measurements close to the trailing edge (10 mm downstream) and from the PIV measurements downstream from the trailing edge ($>$ 50 mm downstream).

The left side of Fig. 13 shows the wake thicknesses above (δ_1) and below (δ_2) of the mean line, and the right side of Fig. 13 shows the total wake thickness $\delta_1 + \delta_2$. Wake thickness is calculated at the location of velocity profile, where

$$U = U_{\min} + 0.5U_{\mathrm{d}} \quad (3)$$

$$U_{\mathrm{d}} = 1 - U_{\min}. \quad (4)$$

The definition of wake thickness is adopted from the study of Thomas and Liu [30], and is sketched in Fig 14. The wake thicknesses based on the minimum

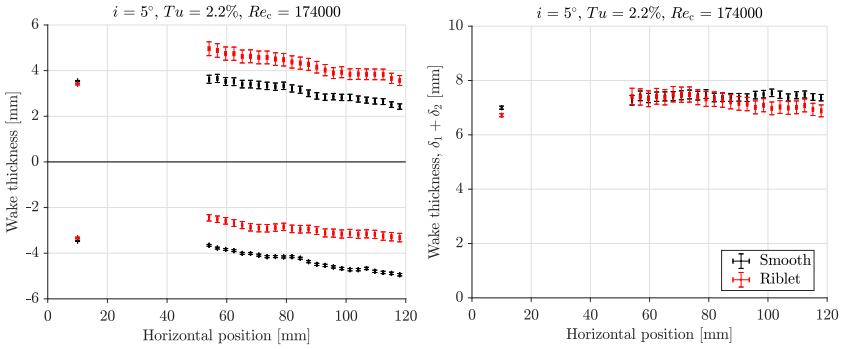

Figure 13: Wake thickness above and below the mean-line (left) and the total wake thickness (right) downstream of the airfoil trailing edge.

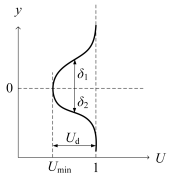

Figure 14: Definition of the wake thicknesses on the airfoil upper side δ_1 and on the lower side δ_2.

velocity are linearly interpolated from the velocity profile. The measurement uncertainties shown in Fig. 13 are based on a confidence interval of 95% and three repeated measurements.

The right side of Fig. 13 shows that the total wake thickness increases with the smooth surface downstream from the trailing edge (location $>$ 90 mm) compared to the riblet surface. The increased wake thickness in the case of the smooth airfoil indicates the mixing out of the wake. The wake of the riblet airfoil is therefore less mixed out due to the reduced turbulence. However, the wake of the riblet airfoil is not wider than that of the smooth airfoil, as was expected in the hypothesis, because the wake thickness on the riblet airfoil pressure side (δ_2) is reduced. The wake thickness decreases on the pressure side when the riblets increase the wake thickness on the suction side in order to fulfill the conservation of mass. The less mixed-out wake caused by the riblets might be insignificant when compared to the wake caused by the entire wind turbine.

3.4. Effect of Riblets on Wind Turbine Power Coefficient and Annual Energy Production

The results above show that the riblets operating near the design incidence are able to reduce drag by up to 6.8%, and the Reynolds stress by up to 80%, which means that the turbulence intensity was reduced by up to around 9%, even though the average angle of the riblet tips was 93% greater than the designed one. This section demonstrates the found drag reduction on the performance of the wind turbine.

The effect of drag reduction on the maximum power coefficient of a horizontal axis wind turbine can be estimated using the equation adopted from the study by Chamorro et al. [14]:

$$C_{\mathrm{p,max}} = \frac{16}{27}\lambda\left(\frac{B^{2/3}}{1.48 + \left(B^{2/3} - 0.04\right)\lambda + 0.0025\lambda^2} - \left(\frac{C_{\mathrm{D}}}{C_{\mathrm{L}}}\right)\frac{1.92B\lambda}{1 + 2B\lambda}\right), \quad (5)$$

where B refers to the number of wind turbine blades, λ to tip speed ratio, and $C_{\mathrm{D}}/C_{\mathrm{L}}$ to drag-to-lift ratio.

The increase in the maximum power coefficient due to the drag reduction is plotted in Fig. 15 at varying tip speed ratios. The maximum power coefficient increases by 4.6% in the case of the three-bladed wind turbine with a tip speed ratio of 8 and drag-to-lift ratio of 0.05. The increase in the maximum power coefficient is 1.7% in the case of the three-bladed wind turbine with a tip speed ratio of 8 and drag-to-lift ratio of 0.025. For an extremely favorable drag-to-lift ratio of 0.005, the power coefficient increase would be only 0.3% due to the riblets. As a comparison, if the highest drag reduction of 16% (reported in the literature for symmetric airfoils) was achieved, the maximum power coefficient could potentially increase by 10.9% in the case of the three-bladed wind turbine with a tip speed ratio of 8 and drag-to-lift ratio of 0.05.

Based on this demonstration, it can be concluded that the effect of riblets on the maximum power coefficient is more significant when the drag-to-lift ratio of the original wind turbine is relatively high. For small HAWTs, the drag-to-lift ratio varies between 0.015 and 0.061 [31], which means that small wind turbines could be a potential application for drag-reducing riblets.

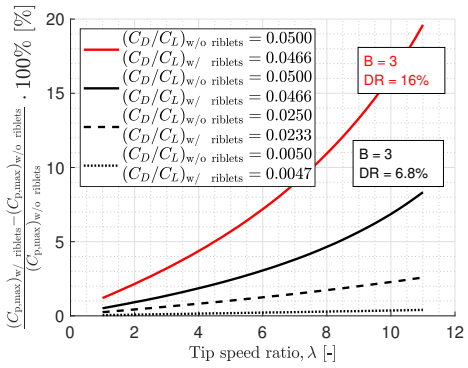

Figure 15: Effect of drag reduction on the maximum power coefficient of a horizontal axis wind turbine with three blades at varying tip speed ratios. B refers to the number of blades and DR to drag reduction.

As a rough estimation for a 15 kW nominal power small wind turbine of Class II (Britwind H15) as described in IEC 61400-2 standard, the annual energy production at an average wind speed of 6 m/s is 2,082 kWh higher with the non-ideally manufactured riblets than it is without them if the maximum power coefficient is increased by 4.6%. As a comparison, the corresponding annual energy production with the high-quality riblets (the drag reduction of 16% as reported in the literature for symmetric airfoils) is 4,933 kWh higher than it is without them if the maximum power coefficient is increased by 10.9%.

In this study, only one airfoil profile (NACA 0024) was analyzed, but in actual wind turbines a range of different airfoil profiles are used. Therefore, the estimations of the effect of riblets on wind turbine power coefficient and energy production are indicative, and the results cannot be generalized without further studies.

4. Conclusions and Outlook

This study concentrated on the effect of nanosecond pulse laser manufactured riblets on the flow field downstream of the symmetric NACA 0024 airfoil. Despite the rough approach for manufacturing the riblets, which resulted in a riblet angle 93% greater than the designed angle, the riblets reduced drag in

the vicinity of the designed incidence by up to 6.8%. It can therefore be concluded that a relatively low-quality riblet structure can be successfully utilized in airfoils, and that the riblet effectiveness is less sensitive to the tip angle than to the height-to-spacing ratio and trapezoidal shape, which were close to the design.

The results from the boundary layer flow field indicated that, at the optimum incidence, the riblets reduced wall shear stress and Reynolds stress, and shifted the velocity profile upwards. It was also found that the turbulence intensity reduction improved with a decreasing Reynolds number. The results from the wake indicated that under their design conditions, the riblets increased the wake thickness on the side of the airfoil where they were located, but decreased the wake thickness on the opposite side of the airfoil, due to the mass conservation. Due to the lower Reynolds stress and turbulence intensity, the mixing out of the wake behind the riblet airfoil was weaker than that of the smooth airfoil.

Even non-ideally manufactured riblets could increase the maximum power coefficient by almost 5% in the case of the three-bladed HAWT with a tip speed ratio of 8 and drag-to-lift ratio of 0.05. The better the drag-to-lift ratio of the original wind turbine, the less significant the effect of riblets on the maximum power coefficient. The results seem promising for small wind turbines that have a low Reynolds number. In the future, it is suggested that a full turbine blade element analysis that includes the effects of riblets would be an important step in order to predict the whole turbine operating map. As the purpose of this study was to demonstrate the effect of riblets on one airfoil profile instead of designing the actual wind turbine, the blade element analysis was not conducted here. It is also suggested that tests with a real wind turbine should be made in the future in order to find the performance potential of low-quality riblets under real operating conditions.

5. Acknowledgements

The authors would like to thank Philipp Gilge M.Sc. and Florian Herbst D.Sc. at Leibniz University Hannover for the riblet design and geometric measurement of the manufactured riblets, and to acknowledge the financial contribution of the Academy of Finland. This research is part of the project funded by the Academy of Finland under grant number 274897.

References

References

[1] R. Lacal-Arántegui, Globalization in the Wind Energy Industry: Contribution and Economic Impact of European Companies, Renewable Energy 134 (2019) 612–628. doi:10.1016/j.renene.2018.10.087.

[2] D. Holst, B. Church, F. Wegner, G. Pechlivanoglou, C. N. Nayeri, C. O. Paschereit, Experimental Analysis of a NACA 0021 Airfoil under Dynamic Angle of Attack Variation and Low Reynolds Numbers, Journal of Engineering for Gas Turbines and Power 141 (2019). doi:10.1115/1.4041146.

[3] D. W. Bechert, M. Bruse, W. Hage, Experiments with Three-Dimensional Riblets as an Idealized Model of Shark Skin, Experiments in Fluids 28 (2000) 403–412. doi:10.1007/s003480050400.

[4] C. Lietmeyer, K. Oehlert, J. R. Seume, Optimal Application of Riblets on Compressor Blades and Their Contamination Behavior, in: Proceedings of the ASME Turbo Expo 2011, 2011, p. 13. Paper No. GT2011-46855. p. 13. June 6–10, 2011, Vancouver, British Columbia, Canada.

[5] D. W. Bechert, M. Bruse, W. Hage, J. G. T. Van der Hoeven, G. Hoppe, Experiments on Drag-Reducing Surfaces and Their Optimization with an Adjustable Geometry, Journal of Fluid Mechanics 338 (1997) 59–87. doi:10.1017/S0022112096004673.

[6] R. García-Mayoral, J. Jiménez, Drag Reduction by Riblets, Philosophical Transactions of the Royal Society A: Mathematical, Physical and Engineering Sciences 369 (2011) 1412–1427. doi:10.1098/rsta.2010.0359.

[7] J. R. Debisschop, F. T. M. Nieuwstadt, Turbulent Boundary Layer in an Adverse Pressure Gradient: Effectiveness of Riblets, AIAA Journal 34 (1996) 932–937.

[8] D. Gatti, M. Quadrio, Reynolds-Number Dependence of Turbulent Skin-Friction Drag Reduction Induced by Spanwise Forcing, Journal of Fluid Mechanics 802 (2016) 553–582. doi:10.1017/jfm.2016.485.

[9] K.-S. Choi, Near-Wall Structure of a Turbulent Boundary Layer with Riblets, Journal of Fluid Mechanics 208 (1989) 417–458. doi:10.1017/S0022112089002892.

[10] J. M. Caram, A. Ahmed, Development of the Wake of an Airfoil with Riblets, AIAA Journal 30 (1992) 2817–2818. doi:10.2514/3.11623.

[11] S. Sundaram, P. R. Viswanath, S. Rudrakumar, Viscous Drag Reduction Using Riblets on NACA 0012 Airfoil to Moderate Incidence, AIAA Journal 34 (1996) 676–682. doi:10.2514/3.13127.

[12] M. Han, H. C. Lim, Y.-G. Jang, S. S. Lee, S.-J. Lee, Fabrication of a Micro-Riblet Film and Drag Reduction Effects on Curved Objects, in: TRANSDUCERS '03. 12th International Conference on Solid-State Sensors, Actuators and Microsystems. Digest of Technical Papers (Cat. No.03TH8664), volume 1, 2003, pp. 396–399. doi:10.1109/SENSOR.2003.1215337.

[13] A. Sareen, R. W. Deters, S. P. Henry, M. S. Selig, Drag Reduction Using Riblet Film Applied to Airfoils for Wind Turbines, in: 49th AIAA Aerospace Sciences Meeting including the New Horizons Forum and Aerospace Exposition, 2011, p. 19. Paper No. AIAA 2011-558, January 4–7, 2011, Orlando, Florida.

[14] L. P. Chamorro, R. E. A. Arndt, F. Sotiropoulos, Drag Reduction of Large Wind Turbine Blades Through Riblets: Evaluation of Riblet Geometry and Application Strategies, Renewable Energy 50 (2013) 1095–1105. doi:10.1016/j.renene.2012.09.001.

[15] C. Lietmeyer, B. Denkena, T. Krawczyk, R. Klin, L. Overmeyer, B. Wojakowski, E. Reithmeier, R. Scheuer, T. Vynnyk, J. R. Seume, Recent Advances in Manufacturing of Riblets on Compressor Blades and Their Aerodynamic Impact, Journal of Turbomachinery 135 (2013). Article ID 041008, 12 p. doi:10.1115/1.4007590.

[16] J. Kaakkunen, J. Tiainen, Jaatinen-Värri, A. A., Grönman, M. Lohtander, Fabrication of Surfaces with Reduced Friction Using Nanosecond Laser, in: Procedia Manufacturing, 28th International Conference on Flexible Automation and Intelligent Manufacturing, FAIM2018, volume 17, 2018, pp. 14–21. doi:10.1016/j.promfg.2018.10.006, May 16–18, 2018, Stockholm, Sweden.

[17] P. R. Spalart, J. D. Mclean, Drag Reduction: Enticing Turbulence, and Then an Industry, Philosophical Transactions of the Royal Society A: Mathematical, Physical and Engineering Sciences 369 (2011) 1556–1569. doi:10.1098/rsta.2010.0369.

[18] P. R. Viswanath, Aircraft Viscous Drag Reduction Using Riblets, Progress in Aerospace Sciences 38 (2002) 571–600. doi:10.1016/S0376-0421(02)00048-9.

[19] F. T. M. Nieuwstadt, W. Wolthers, H. Leijdens, K. Krishna Prasad, A. Schwarz-van Manen, The Reduction of Skin Friction by Riblets Under the Influence of an Adverse Pressure Gradient, Experiments in Fluids 15 (1993) 17–26. doi:10.1007/BF00195591.

[20] C. Lietmeyer, K. Oehlert, J. R. Seume, Optimal Application of Riblets on Compressor Blades and Their Contamination Behavior, Journal of Turbomachinery 135 (2012). doi:10.1115/1.4006518.

[21] Y. Wang, S. Shen, G. Li, D. Huang, Z. Zheng, Investigation on Aerodynamic Performance of Vertical Axis Wind Turbine with Different Series Airfoil Shapes, Renewable Energy 126 (2018) 801–818. doi:10.1016/j.renene.2018.02.095.

[22] S. Barbarelli, G. Florio, G. Lo Zupone, N. M. Scornaienchi, First Techno-Economic Evaluation of Array Configuration of Self-Balancing Tidal Kinetic Turbines, Renewable Energy 129 (2018) 183–200. doi:10.1016/j.renene.2018.06.007.

[23] J. B. Barlow, W. H. Rae Jr., A. Pope, Low-Speed Wind Tunnnel Testing, John Wiley & Sons, 1999. p. 713. ISBN 978-81-265-2568-3.

[24] M. V. Casey, C. J. Robinson, A Unified Correction Method for Reynolds Number, Size, and Roughness Effects on the Performance of Compressors, Proceedings of the Institution of Mechanical Engineers, Part A: Journal of Power and Energy 225 (2011) 864–876. doi:10.1177/0957650911410161.

[25] J. Kaakkunen, J. Tiainen, Jaatinen-Värri, A. A., Grönman, M. Lohtander, Nanosecond Laser Ablation of the Trapezoidal Structures for Turbomachinery Applications, in: Procedia Manufacturing, 8th Swedish Production Symposium, SPS 2018, volume 25, 2018, pp. 435–442. doi:10.1016/j.promfg.2018.06.114, Paper ID 1132. June 11–14, 2018, Columbus, OH, USA.

[26] G. Ren, J. Liu, J. Wan, F. Li, Y. Guo, D. Yu, The Analysis of Turbulence Intensity Based on Wind Speed Data in Onshore Wind Farms, Renewable Energy 123 (2018) 756–766. doi:10.1016/j.renene.2018.02.080.

[27] K. S. Hansen, R. J. Barthelmie, L. E. Jensen, A. Sommer, The Impact of Turbulence Intensity and Atmospheric Stability on Power Deficits Due to Wind Turbine Wakes at Horns Rev Wind Farm, Wind Energy 15 (2012) 183–196. doi:10.1002/we.512.

[28] S.-J. Lee, Y.-S. Choi, Decrement of Spanwise Vortices by a Drag-Reducing Riblet Surface, Journal of Turbulence 9 (2008) 1–15. doi:10.1080/14685240802251517.

[29] E. Moreau, Airflow Control by Non-Thermal Plasma Actuators, Journal of Physics D: Applied Physics 40 (2007) 605–636. doi:10.1088/0022-3727/40/3/S01.

[30] F. O. Thomas, X. Liu, An Experimental Investigation of Symmetric and Asymmetric Turbulent Wake Development in Pressure Gradient, Physics of Fluids 16 (2004) 1725–1745. doi:10.1063/1.1687410.

[31] R. K. Singh, M. R. Ahmed, M. A. Zullah, Y.-H. Lee, Design of a Low Reynolds Number Airfoil for Small Horizontal Axis Wind Turbines, Renewable Energy 42 (2012) 66–76. doi:10.1016/j.renene.2011.09.014.